remote sensing

MDPI

Article

Spatiotemporal Patterns and Drivers of Multiple Forest Change Types in China's Tropical and Subtropical Regions

Yikang Wang [1,2], Zhiyong Wu [3], Ping He [3], Mingxing Zhou [1,2], Dengsheng Lu [1,2] and Dengqiu Li [1,2,*]

[1] Fujian Provincial Key Laboratory for Subtropical Resources and Environment, Fujian Normal University, Fuzhou 350007, China
[2] Institute of Geography, Fujian Normal University, Fuzhou 350007, China
[3] Fujian Forestry Prospect and Design Institute, Fuzhou 350001, China
* Correspondence: lidengqiu@fjnu.edu.cn

Highlights

What are the main findings?

- A unified 29-year (1993–2021) multi-type forest-change dataset for tropical and subtropical China reveals that fire and clear-cutting exhibit a southeast–southwest dual-core spatial pattern, while afforestation and deforestation show congruent, largely dispersed distributions dominated by the moderate period-summary intensity class.
- Fire shows an overall declining trend, clear-cutting increases significantly, and both afforestation and deforestation are dominated by increasing trends. The annual intensity-class models identify potential evapotranspiration and mean temperature as important predictors for fire and clear-cutting, respectively, while slope and population are important predictors for both afforestation and deforestation. Slope is a prominent negative SHAP contributor to the annual high-intensity class output, particularly for afforestation and deforestation.

What are the implications of the main findings?

- The XGBoost–SHAP framework captures nonlinear associations with annual forest-change intensity classes and maps dominant positive and negative contributors to the annual high-intensity class output, providing information for regional forest management and climate-adaptive ecological policy design.
- The concurrent analysis of multiple forest change types in a unified framework provides a more comprehensive understanding of forest dynamics than single-process studies, supporting integrated planning for both forest protection and ecological restoration in subtropical ecosystems.

Abstract

Tropical and subtropical forests harbor over half of the world's terrestrial biodiversity and account for a large fraction of the global terrestrial carbon sink. However, under accelerating climate change and human pressure, the dynamics of these forests remain incompletely characterized, particularly in rapidly developing regions where multiple change processes—fire, clear-cutting, afforestation, and deforestation—operate simultaneously. Using 30 m Landsat time-series imagery spanning 1993–2021, fused with China's annual land-cover dataset (CLCD) and the continuous change-detection algorithm (CCDC), this study constructed a unified, multi-type forest-change dataset for tropical and subtropical China. The spatiotemporal patterns of four dominant change types were quantified through grid-based intensity analysis and the Mann–Kendall trend test, and associations with annual intensity classes were examined using an eXtreme Gradient Boosting (XGBoost) ensemble learner combined with SHapley Additive exPlanations (SHAP) model interpretation. Our results reveal

Check for updates

Academic Editor: Ricardo Dalagnol

Received: 8 October 2026
Revised: 6 November 2026
Accepted: 12 November 2026
Published: 17 November 2026

Copyright: © 2026 by the authors. Licensee MDPI, Basel, Switzerland. This article is an open access article distributed under the terms and conditions of the Creative Commons Attribution (CC BY) license.

the following: First, spatially, fire and clear-cutting both exhibit a southeast–southwest dual-core aggregation pattern, while afforestation and deforestation show highly congruent, largely dispersed distributions dominated by the moderate period-summary intensity class. Second, temporally, fire shows an overall declining trend, with 52.1% of grid cells exhibiting significant or non-significant decreases; clear-cutting shows significant increases in 28.4% of grid cells. Afforestation and deforestation are both dominated by significant and non-significant increases: 48.7% and 62.8% of grid cells, respectively. For deforestation, 44.8% of the grids included in the peak-year analysis reached their maximum annual intensity during 2011–2015, although this concentration may partly reflect temporal inconsistencies in the underlying CLCD data. Third, the annual intensity-class models identify potential evapotranspiration as a leading predictor for fire and mean temperature as an important environmental covariate for clear-cutting. Slope and population are important predictors for both afforestation and deforestation. In the spatial summaries of SHAP contributions to the annual high-intensity class output, slope is a prominent negative contributor, particularly for afforestation and deforestation. This study provides a unified, multi-type, multi-decade analysis of forest change in tropical and subtropical China, characterizes nonlinear associations with annual intensity-class outputs, and maps their dominant positive and negative SHAP contributors to support precision forest management and climate-adaptive ecological policy design.

Keywords: forest change types; spatiotemporal patterns; driving factors; XGBoost–SHAP; China's tropical and subtropical

1. Introduction

Forest ecosystems cover approximately 30% of Earth's land surface and contribute a large share of terrestrial biodiversity, carbon sequestration, hydrological regulation, and livelihood support [1,2]. Among forest biomes, tropical and subtropical forests are of particular scientific and policy significance: although they occupy only about 12% of global land area, they harbor more than half of all terrestrial species and drive much of the interannual variability of the global carbon sink [3,4]. Therefore, quantifying the dynamics of these forests and the mechanisms behind them is essential for both fundamental ecology and global-change science.

Under intensifying climate change and human land use, tropical and subtropical forests are undergoing rapid and multifaceted changes. Climate-driven shifts in temperature and precipitation regimes have extended fire seasons and amplified burn severity in many regions [5,6]. Economic development and policy interventions simultaneously drive forest loss (e.g., deforestation, clear-cutting) and forest gain (e.g., plantation establishment, afforestation programs), generating a complex mosaic of forest dynamics that is poorly described by any single change type alone [7–9]. A coherent picture of multi-type forest change thus requires an integrated analytical framework that can disentangle the spatial and temporal fingerprints of each process and attribute them to specific drivers.

China's tropical and subtropical forests represent a globally significant component of this biome. Spanning approximately 2.4 million km^2 across 15 provinces, these forests form a contiguous ecological barrier that modulates regional climate and supports exceptional species diversity [10]. As a hotspot of both ecological importance and rapid economic development, the region has experienced dramatic land-use transitions during the past three decades—including large-scale ecological restoration programs, expanding fast-growing timber plantations, and accelerating urbanization [11,12]. These transitions operate concurrently with

increasingly frequent climate-related disturbances, creating a complex, multi-process dynamic that has rarely been addressed in a unified analytical framework.

Previous studies of forest change in China's tropical and subtropical regions have generally focused on individual change processes. Forest fire research documents pronounced spatiotemporal heterogeneity linked to meteorological and socioeconomic drivers [13–15]. Clear-cutting studies report concentration in plantation-rich provinces such as Guangxi and Jiangxi, with increasing trends since the 1990s [16]. Afforestation studies confirm China as a major contributor to global greening [7,17], and deforestation studies identify agricultural expansion and plantation development as dominant drivers [18,19]. Although valuable, these process-specific studies cannot reveal the relative importance, spatial co-occurrence, or divergent drivers of simultaneous forest change processes—leaving a critical gap in understanding.

Beyond thematic fragmentation, a methodological limitation persists. Most existing studies rely on traditional statistical frameworks—such as ordinary least-squares regression, geographically weighted regression, or logistic regression—that inherently assume linear or locally linear relationships between drivers and forest-change outcomes. This assumption is problematic because forest-change processes frequently exhibit nonlinear threshold responses, complex factor interactions, and long-tailed intensity distributions [18]. Ensemble machine-learning algorithms, paired with model-agnostic interpretation tools such as SHapley Additive exPlanations (SHAP) values, offer a robust alternative: they accommodate high-dimensional predictor spaces, capture nonlinear threshold effects, and permit spatially explicit attribution of dominant drivers and inhibitors [20–22]. However, these tools have rarely been deployed for multi-type forest-change analysis in China's subtropical context.

Against this background, this study advances the investigation of tropical and subtropical forest dynamics by addressing three specific objectives: (i) to construct a unified, high-accuracy, long-term (1993–2021) forest-change dataset covering four major change types—fire, clear-cutting, afforestation, and deforestation—by integrating multi-source remote-sensing products within a spatiotemporal filtering framework; (ii) to systematically examine the spatiotemporal patterns and temporal evolution of the four change types using grid-based intensity quantification and nonparametric trend analysis; and (iii) to conduct a comprehensive, nonlinear driver analysis using an eXtreme Gradient Boosting (XGBoost)–SHAP framework, with specific emphasis on spatially explicit visualization of SHAP contributions to the annual high-intensity class output.

2. Materials and Methods

2.1. Study Area

The study focuses on tropical and subtropical China, a region spanning approximately 2.4 million km^2 across 15 provinces and municipalities (Shanghai, Jiangsu, Zhejiang, Anhui, Fujian, Jiangxi, Hunan, Guizhou, Guangxi, Hubei, Chongqing, Guangdong, Yunnan, Sichuan, and Hainan) (Figure 1). The region is dominated by subtropical monsoon and tropical monsoon climates, with annual precipitation of 1300–2000 mm and mean annual temperature of 15–22 °C. Pronounced topographic relief generates strong climatic vertical differentiation and diverse ecosystem types, ranging from lowland tropical rainforest and monsoon forest through mid-elevation subtropical evergreen broadleaf forest to high-elevation temperate coniferous forest [10,23]. The region is economically developed and densely populated, and rapid urbanization and large-scale population migration have generated substantial pressures on forest resources [11,24]. The forest distribution shown in Figure 1 was derived from pixels classified as forest in the 2020 China Land Cover Dataset (CLCD), clipped to the boundary of tropical and subtropical China.

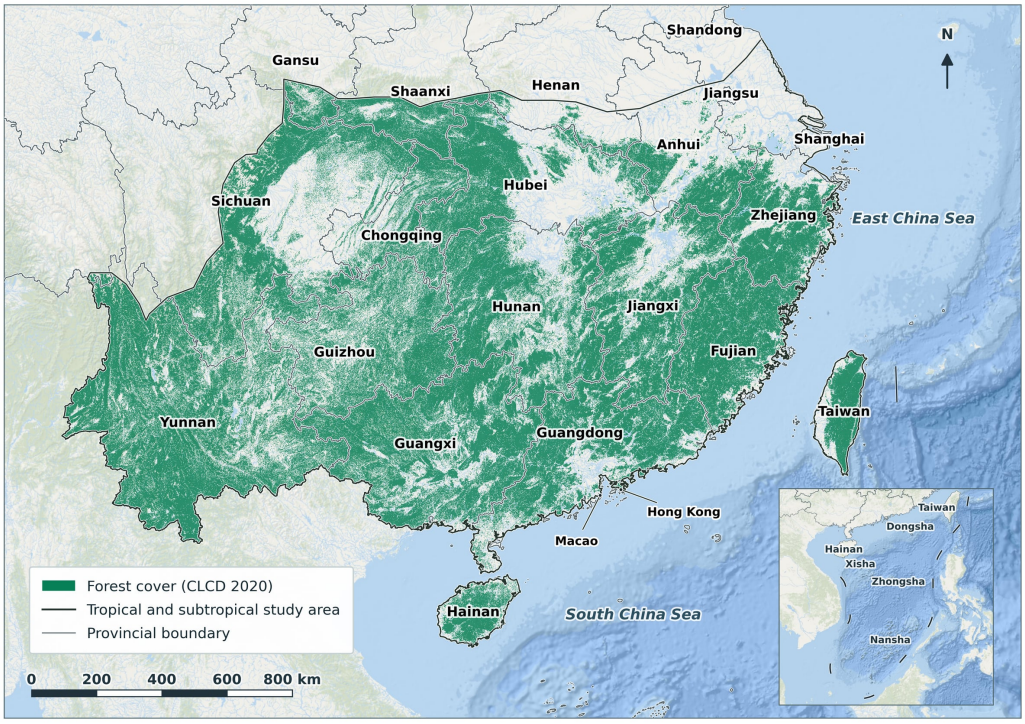

Figure 1. Spatial distribution of forests in China's tropical and subtropical regions in 2020.

2.2. Data Sources and Preprocessing

2.2.1. Forest Remote Sensing Products

CCDC used individual Landsat Collection 2 surface reflectance observations at their original acquisition dates. Clouds and cloud shadows were masked in Google Earth Engine using the QA_PIXEL band. We analyzed disturbance records for 1993–2021. Annual forest/non-forest classification was derived from the China Land Cover Dataset (CLCD), which provides annual land-cover maps for China at 30 m resolution for 1990–2024 [11]. The CLCD categorizes the land surface into nine primary classes—cropland, forest, shrubland, grassland, water body, snow/ice, barren land, impervious surface, and wetland. CLCD provides reliable and temporally consistent 30 m annual land-cover information, supporting the identification of persistent forest/non-forest transitions and the subsequent derivation of afforestation and deforestation classes. Because no independent long-term nationwide reference dataset was available for these two change types, separate sample-based validation was not conducted.

2.2.2. Forest-Change Driver Variables

The explanatory variables (Table 1) were selected to represent four commonly recognized dimensions of forest-change processes: climatic constraints, topographic controls, vegetation condition, and human disturbance pressure. Climatic variables—including precipitation, temperature, dryness, potential evapotranspiration (PET), and wind speed—represent hydrothermal conditions, fuel moisture, fire risk, and forest productivity. Elevation, slope, and aspect capture topographic controls on accessibility, erosion risk, land-use suitability, and microclimate. NDVI was included as a proxy for vegetation productivity and greenness, while road-network density and population size represent anthropogenic accessibility and pressure associated with harvesting, land conversion, and restoration. Several potential drivers, such as forest ownership and tenure-reform intensity, timber prices, and market demand, were not included because long-term, spatially explicit, and temporally consistent data were unavailable.

Table 1. Variables for driver analysis of forest change.

Data Type	Description	Time	Original Resolution	References/URL (Date Accessed)	Source
Climatic	Annual Dryness	1993–2021	1 km	(http://www.nesdc.org.cn/, 10 January 2025)	National Ecological Data Center
	Annual average potential evapotranspiration	1993–2021	1 km	[25]	
	Annual Precipitation	1993–2021	1 km	[26]	National Tibetan Plateau Data Center
	Annual Average Temperature	1993–2021	1 km		
	Annual Maximum Temperature	1993–2021	1 km		
	Annual Minimum Temperature	1993–2021	1 km		
	Annual Average Wind Speed	1993–2021	0.1°	[27]	ERA5-Land
Topographic	Elevation	Static	30 m	(http://www.gscloud.cn/, 13 September 2025)	Geospatial Data Cloud
	Slope				
	Aspect				
Vegetation	NDVI	1993–2021	0.05°	[28]	NOAA AVHRR NDVI CDR V5
Socio-economic	Road Network	2018; treated as static throughout 1993–2021		[29]	GRIP4 Global Road Dataset
	Population Density	1993–2021	30 arc-sec	[30]	GlobPOP Dataset

All explanatory variables were summarized within the same predefined 0.2° × 0.2° analysis grids in the WGS84 geographic coordinate reference system (EPSG:4326). Input rasters were retained at their existing spatial resolutions during feature extraction. Where the grid and raster CRSs differed, the grid polygons were transformed to the corresponding raster CRS before zonal statistics were calculated. Predictor values were subjected to Winsorization at the 1st and 99th percentiles, followed by z-score standardization. Maximum, minimum, mean, and standard deviation were extracted for each of the 13 explanatory variables within each grid, yielding 52 statistical features. Annual climate, NDVI, and population data were matched to the forest-change response for the same year and the same 0.2° grid cell. Elevation, slope, aspect, and road density were treated as static covariates, with the same spatial layer for each variable used across all years. Road density was derived from the 2018 road network.

2.3. Methodology

The analytical workflow comprises three integrated modules (Figure 2). First, a multi-type forest-change dataset was constructed by integrating CLCD-derived land-cover transitions and forest-disturbance records within a spatiotemporal filtering framework. Second, grid-based intensity quantification and the Mann–Kendall trend test were applied to characterize the spatiotemporal patterns of the four change types. Third, an XGBoost ensemble learner, combined with SHAP model interpretation, was trained to identify the driving

factors and nonlinear driver–response relationships. The following subsections describe each module in detail.

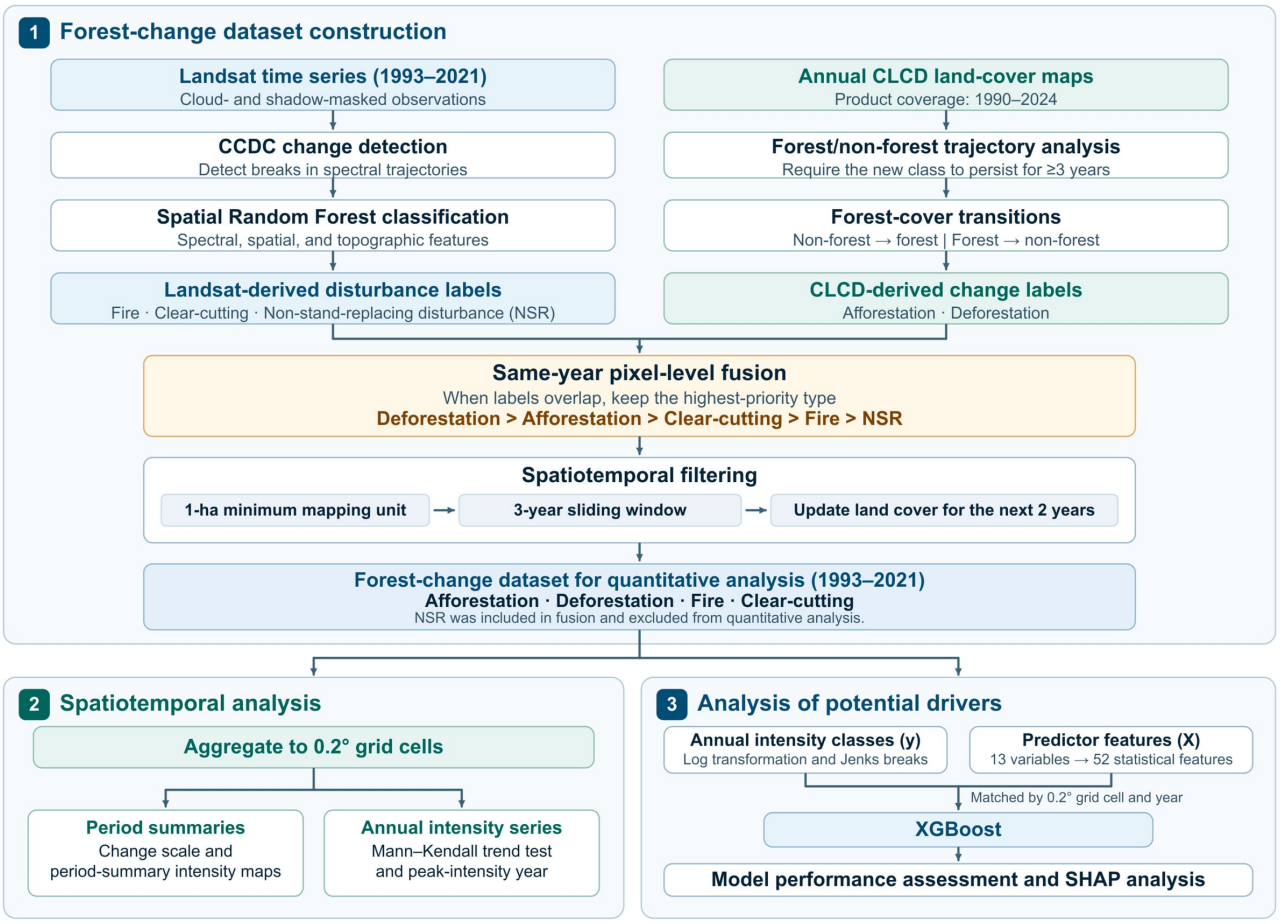

Figure 2. Technical workflow of this study.

2.3.1. Construction of the Multi-Type Forest-Change Dataset

(1) Afforestation and Deforestation Identification

Following established forest-cover change methodologies [31] and annual land cover products spanning 1990–2024, we defined afforestation as a transition from non-forest to forest that remains classified as forest for at least three consecutive years, and deforestation as a transition from forest to non-forest that remains non-forest for at least three consecutive years (Figure 3). Pixels whose land-cover class in a given year was identical to that of the preceding year were classified as unchanged. This three-year persistence criterion effectively reduces spurious transitions caused by short-term fluctuations in spectral signals.

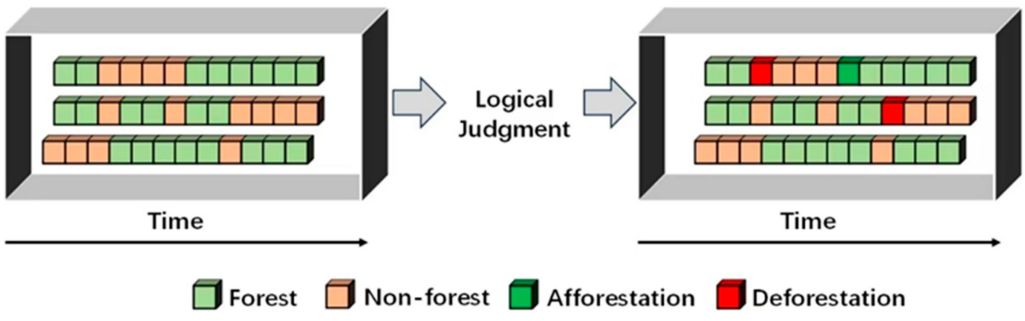

Figure 3. Identification rules for deforestation and afforestation.

(2) Fire and Clear-Cutting Attribution

To detect stand-replacing forest disturbances—specifically fire and clear-cutting—we applied the Continuous Change Detection and Classification (CCDC) algorithm to the Landsat time series. CCDC detects statistically significant breaks in temporal spectral trajectories, which were then attributed to specific disturbance types using a spatial Random Forest (sRF) classifier trained on reference samples [16]. CCDC flagged a breakpoint when four consecutive observations deviated significantly from the fitted model. Sparse clear observations may have led to missed or delayed detections. Reference samples were collected from multiple sources, including literature review, visual interpretation of high-resolution imagery, field surveys, and forest-management inventory records.

During training, 438 disturbance patches—comprising 265 clear-cutting, 98 fire, and 75 non-stand-replacing disturbance events—were identified through restricted randomized sampling integrated with high-resolution imagery, Landsat time-series data, and MODIS fire products (FireCCI51). To ensure spectral diversity and maintain sample balance among the three classes, 9225 labeled pixels were selected from within these 438 reference patches as pixel-level training samples for the sRF classifier. The number of decision trees (ntree) was set to 200, and all other parameters were retained at their default values. Feature variables included spectral indices (e.g., Normalized Burn Ratio (NBR), Near-Infrared (NIR), and Short-Wave Infrared 1 (SWIR1)), spatial features, and topographic features [16]. After pixel-level prediction, the final classification of each disturbance patch was determined by the mode of its internal pixel predictions, thereby aggregating pixel-level uncertainty to the more ecologically meaningful patch scale.

Accuracy validation was conducted using stratified random sampling. A total of 1663 samples were selected—comprising 569 non-stand-replacing disturbances, 234 fire events, and 860 clear-cutting instances—to evaluate disturbance-type classification accuracy. Each sample was manually interpreted by integrating Landsat time-series, high-resolution imagery, and auxiliary datasets. To ensure independence and objectivity, interpreters were blinded to the model's disturbance detection and classification results. A sample was deemed correctly identified only if the reference data and the model product were consistent in both disturbance type and occurrence year (within a permissible ±1-year window); otherwise, it was categorized as a commission error, omission error, or temporal error. User's Accuracy (UA), Producer's Accuracy (PA), and Overall Accuracy (OA) were computed for each disturbance type.

(3) Multi-source Change Information Fusion

To construct the unified forest-change dataset, the forest-disturbance data (fire, clear-cutting, and non-stand-replacing disturbance) were fused with the CLCD-derived afforestation and deforestation layers. A priority-based, pixel-by-pixel fusion was performed according to the following hierarchy: deforestation > afforestation > clear-cutting > fire > non-stand-replacing disturbance. If a pixel was flagged by multiple change types in the same year, the type with the highest priority was retained; otherwise, the individual detection result was adopted directly. Non-stand-replacing disturbances were excluded from quantitative analysis because of their heterogeneous etiology. To enhance temporal consistency and accuracy, the initial fusion results underwent additional spatiotemporal filtering: (i) isolated noise pixels were removed by enforcing a minimum mapping unit (MMU) of 1 ha; (ii) a three-year sliding window was applied to suppress repeated disturbance signals, recording only the highest-priority type within the window; and (iii) the land-cover status for the subsequent two years was updated following each disturbance event (e.g., a deforestation event forced the pixel to be labeled as non-forest for two years). This multi-step filtering avoids misidentifying a single continuous disturbance process as multiple independent events. To assess the potential influence of the priority-based fusion,

we quantified same-year multi-type overlaps. Overlapping pixels accounted for 1.32% of the changed pixels (flagged by at least one change type) and 0.02% of all valid pixels. Thus, priority assignment affected only a small proportion of observations, supporting the robustness of the fused forest-change dataset.

Table 2 summarizes the operational definitions of the four forest-change types. Afforestation and deforestation represent persistent non-forest-to-forest and forest-to-non-forest transitions, respectively, lasting for at least three consecutive years; in contrast, clear-cutting and fire are stand-replacing disturbances that may be followed by forest recovery or replanting. Thus, "deforestation" is used here in a narrow land-cover-transition sense rather than as an umbrella term for all forest loss. Together, these mutually exclusive categories integrate observable transition trajectories and disturbance mechanisms into a remote-sensing classification scheme for tropical and subtropical China.

Table 2. Definitions of forest change types in this study.

Change Type	Definition
Afforestation	A transition from non-forest to forest that remains classified as forest for at least three consecutive years.
Deforestation	A transition from forest to non-forest that remains classified as non-forest for at least three consecutive years.
Clear-cutting	A stand-replacing disturbance attributed to clear-cutting within forest areas and not classified as deforestation.
Fire	A stand-replacing disturbance attributed to fire within forest areas and not classified as deforestation.

2.3.2. Spatiotemporal Distribution Patterns of Forest Change

(1) Grid-based Quantification of Forest Change Scale and Intensity

For comparable spatial quantitative analysis, the study area was partitioned into 0.2° regular spatial grids, and two complementary metrics—change scale and change intensity—were computed at the grid scale. Forest change scale was defined as the total area of forest change within each grid cell, normalized by the maximum and minimum grid values (Equation (1)). Period-summary forest-change intensity was calculated as the sum of annual change areas divided by the sum of corresponding annual forest areas within each grid cell during 1993–2021 (Equation (2)). This metric summarizes annual intensity using annual forest area as the weight and was used to characterize long-term spatial patterns. Intensity, rather than scale, was selected as the primary metric for characterizing disturbance dynamics because baseline forest area varies substantially across the study region; the intensity index accounts for differences in forest extent, facilitating comparisons across grid cells and providing a more ecologically meaningful characterization of forest degradation, recovery, and transformation.

$$S_i = \frac{A_{dist,i} - A_{min}}{A_{max} - A_{min}} \times 100\% \quad (1)$$

$$I_i^{map} = \frac{\sum_{t=1993}^{2021} A_{i,t}}{\sum_{t=1993}^{2021} F_{i,t}} \quad (2)$$

where S_i is the forest-change scale index; $A_{dist,i}$ is the total forest-change area in grid i; and A_{max} and A_{min} are the maximum and minimum grid-level change areas across the study area. I_i^{map} is the period-summary forest-change intensity (%); $A_{i,t}$ is the area of a given change type in grid i and year t; and $F_{i,t}$ is the corresponding annual forest area.

The forest-change data exhibit a distinct long-tailed distribution: most grids experience minimal change, while a small fraction undergo extensive change. Accordingly, a logarithmic transformation was applied to reduce positive skewness, followed by Jenks natural-breaks classification to categorize the period-summary indicators into three ordinal

classes: high, moderate, and low. This classification approach maximizes between-class variance and minimizes within-class variance, making it well suited to spatially explicit ecological data with non-normal distributions.

(2) Characterizing Temporal Trends of Four Forest Change Types

Temporal trends in the annual continuous intensity series (Equation (3)) of the four forest-change types for 1993–2021 were analyzed using the Mann–Kendall (MK) nonparametric test. Unlike parametric trend tests, the MK test does not require data to follow a specific distribution and is robust against outliers, rendering it particularly suitable for trend detection in long-term environmental time series. The direction of temporal trends was determined by the standardized MK test statistic (Z), and statistical significance was evaluated using the *p*-value with $\alpha = 0.05$ as the threshold. Based on the resulting statistics, temporal trends of forest-change intensity at the grid scale were classified into five categories: significant increase, non-significant increase, no significant trend, non-significant decrease, and significant decrease. To further elucidate the local temporal characteristics of forest-change dynamics, the year of most severe change for each grid cell was identified as the year exhibiting the maximum forest-change intensity within the study period. For visualization, peak-intensity years were grouped into calendar-aligned intervals: 1993–2000, 2001–2005, 2006–2010, 2011–2015, and 2016–2021. The endpoint intervals retained all available years at the beginning and end of the study period. These intervals contain 8, 5, 5, 5, and 6 years, respectively. Their grouped percentages summarize the timing of grid-level maxima and were not normalized by interval duration. Significant increases and decreases were defined as $Z > 0$ and $Z < 0$, respectively, with $p < 0.05$. Non-significant increases and decreases were defined as $Z > 0$ and $Z < 0$, respectively, with $p \geq 0.05$. The No trend category comprised non-constant series with $Z = 0$ and constant annual-intensity series. Because Sen's slope or another rate estimator was not calculated, interpretation was restricted to trend direction and statistical significance rather than change magnitude or annual rate of change.

2.3.3. Drivers Analysis of Forest Change

For model training, annual forest-change intensity was calculated separately for each grid-year observation as the mapped area of a given change type in that year divided by the corresponding annual forest area:

$$I_{i,t}^{annual} = \frac{A_{i,t}}{F_{i,t}} \quad (3)$$

where $I_{i,t}^{annual}$ is the annual forest-change intensity (%) in grid *i* and year t; $A_{i,t}$ is the mapped area of a given forest-change type in that grid and year; and $F_{i,t}$ is the corresponding annual forest area. The calculation was performed separately for each change type over 1993–2021.

For each change type, positive annual intensities pooled across grid-year observations were log-transformed and classified into three intensity classes using Jenks natural breaks. These classes served as the response variable. The modeling data therefore used annually matched forest-area denominators, rather than the period-summary intensity shown in the maps. The annual model-response classes and period-summary map classes were derived independently using separate thresholds and are not interchangeable. Temporal trends and the timing of grid-level intensity maxima were derived from the annual continuous intensity series. All class-specific SHAP interpretations below refer to the annual model-response classes, whereas the period-summary intensity classes were derived separately using the thresholds reported in Table S2. The response and the annually available explanatory variables were matched by both grid location and year, while the topographic variables and the 2018 road-density layer were held constant across years for the corresponding grids. An XGBoost ensemble learning algorithm was employed to model associations between the explanatory variables and annual forest-change intensity classes [32]. Rooted in the

gradient-boosted decision-tree paradigm, XGBoost iteratively constructs classification and regression tree (CART) base learners, where each new tree is trained to fit the residual errors of the preceding ensemble, progressively improving predictive accuracy and generalization. XGBoost additionally introduces a regularization term in its objective function to penalize overly complex tree structures, rendering it robust to overfitting in high-dimensional ecological predictor spaces.

Model training was implemented with ten independent repeated experiments to ensure robustness. In each run, the random seed was re-initialized, and stratified random sampling was applied to split the dataset into training and testing subsets at a 7:3 ratio, preserving the proportional distribution of intensity categories in each subset. Rather than relying on a single optimal training result, model performance was summarized using the mean and standard deviation across the ten trials. Based on preliminary hyperparameter tuning, the key parameters were set as follows: learning rate (eta) = 0.084, maximum tree depth = 12, and maximum iterations = 3000. An early-stopping strategy was integrated to terminate training if validation loss showed no significant improvement over 50 consecutive epochs. Model performance was evaluated using four metrics: Overall Accuracy (OA), the Kappa coefficient, multi-class Area Under the Curve (AUC), and the macro-F1 score.

To address the inherent 'black-box' challenge of ensemble learning models, the SHapley Additive exPlanations (SHAP) method [33] was employed to interpret the XGBoost predictions. SHAP provides a game-theoretic framework for attributing individual model predictions to input features. For a given intensity class, positive and negative SHAP values represent contributions that increase and decrease the model output relative to its baseline, respectively. Using the trained optimal XGBoost model, global feature importance—defined as the mean absolute SHAP value across all samples for a given feature—was computed to rank the natural-geographical and socioeconomic factors and identify the variables contributing most strongly to the model predictions. Beyond global ranking, SHAP dependence plots were constructed to examine nonlinear patterns in feature contributions to the high-intensity class output. Changes in the direction or magnitude of these contributions were interpreted as model response features that may inform ecological hypotheses.

Building on this interpretation framework and the intensity classification derived from log-transformation and Jenks natural breaks, this study focuses on SHAP contributions to the high-intensity class output. Spatial patterns of dominant positive and negative model contributions were summarized at the analysis-grid scale using the class-specific SHAP feature vectors (Table 3). This complements global feature-importance rankings by describing spatial variation in the fitted relationships and providing information for further ecological interpretation.

Table 3. Definitions of dominant positive and negative SHAP contributors to the annual high-intensity class output.

Factor Category	Definition	Ecological Meaning
Dominant positive SHAP contributor	Feature with the largest positive SHAP contribution to the annual high-intensity class output	Largest upward contribution to that class output relative to its baseline
Dominant negative SHAP contributor	Feature with the most negative SHAP contribution to the annual high-intensity class output	Largest downward contribution to that class output relative to its baseline

3. Results

3.1. Accuracy Assessment of Forest-Change-Type Classification

Validation results indicate an Overall Accuracy (OA) of 79.6% for the combined spatiotemporal and categorical consistency of the forest-change classification (Table 4). The model demonstrates robust identification performance for clear-cutting and non-stand-replacing disturbances, whereas fire detection accuracy is comparatively lower. Specifically, for non-stand-replacing disturbances, User's Accuracy (UA = 88.8%) exceeds Producer's Accuracy (PA = 73.7%), indicating that most pixels labeled as non-stand-replacing disturbances are correctly identified but that a non-negligible fraction of true events are missed, with most misclassifications being assigned to clear-cutting. Conversely, clear-cutting exhibits higher PA (91.5%) than UA (76.4%), indicating a modest commission error. For fire events, the PA and UA are comparable, and both exceed 61%, indicating roughly symmetric commission and omission errors—consistent with the inherent difficulty of mapping small, fast-growing fire events in a heterogeneous subtropical landscape. These accuracy levels are comparable to or exceed published multi-type disturbance mapping studies in comparable subtropical regions [16,34], supporting the reliability of the subsequent quantitative analyses.

Table 4. Accuracy assessment of forest change types.

Predicted Change Class	Reference			UA (%)
	Non-Clear-Cutting	Clear-Cutting	Fire	
Non-clear-cutting	505	41	23	88.8
Clear-cutting	127	657	76	76.4
Fire	53	20	161	68.8
PA (%)	73.7	91.5	61.9	OA (%): 79.6

3.2. Spatiotemporal Patterns of Forest Change Types

3.2.1. Spatial Distribution Patterns

The four forest change types differ markedly in spatial scale structure and aggregation patterns (Figure 4). Forest fire is characterized by distinct low-scale clustering (accounting for 55.9% of all grids), with high-scale occurrences concentrated in two core zones: the southern coastal belt and the border plateau regions. Clear-cutting shows relatively balanced proportions across three scale grades (with low, moderate, and high scales accounting for 35.4%, 32.0%, and 32.6%, respectively) and a broader "southeast–southwest dual-core" spatial structure. Afforestation is dominated by low and moderate scales (39.0% and 36.4%) with weak high-scale aggregation, displaying scattered distribution across multiple regional centers. Deforestation exhibits a unique moderate-scale dominant pattern (47.6%), highly similar to afforestation, with concentrated high-scale centers and widespread moderate-scale coverage across most of the region.

The mapped distributions of forest-change scale and period-summary intensity show broad spatial correspondence, with large-scale change zones generally coinciding with high-intensity areas (Figures 4 and 5). Fire displays relatively balanced period-summary intensity distributions, with moderate and high classes accounting for 40.8% and 34.7% of grids, respectively. The high class accounts for the largest proportion of clear-cutting grids (46.7%). Afforestation and deforestation are concentrated in the moderate period-summary intensity class (46.4% and 60.8%, respectively). The high class accounts for 16.3% of afforestation grids and 26.2% of deforestation grids, compared with 34.7% for fire

and 46.7% for clear-cutting. Because classes were defined separately for each change type, identical class labels do not imply identical absolute intensity values across change types.

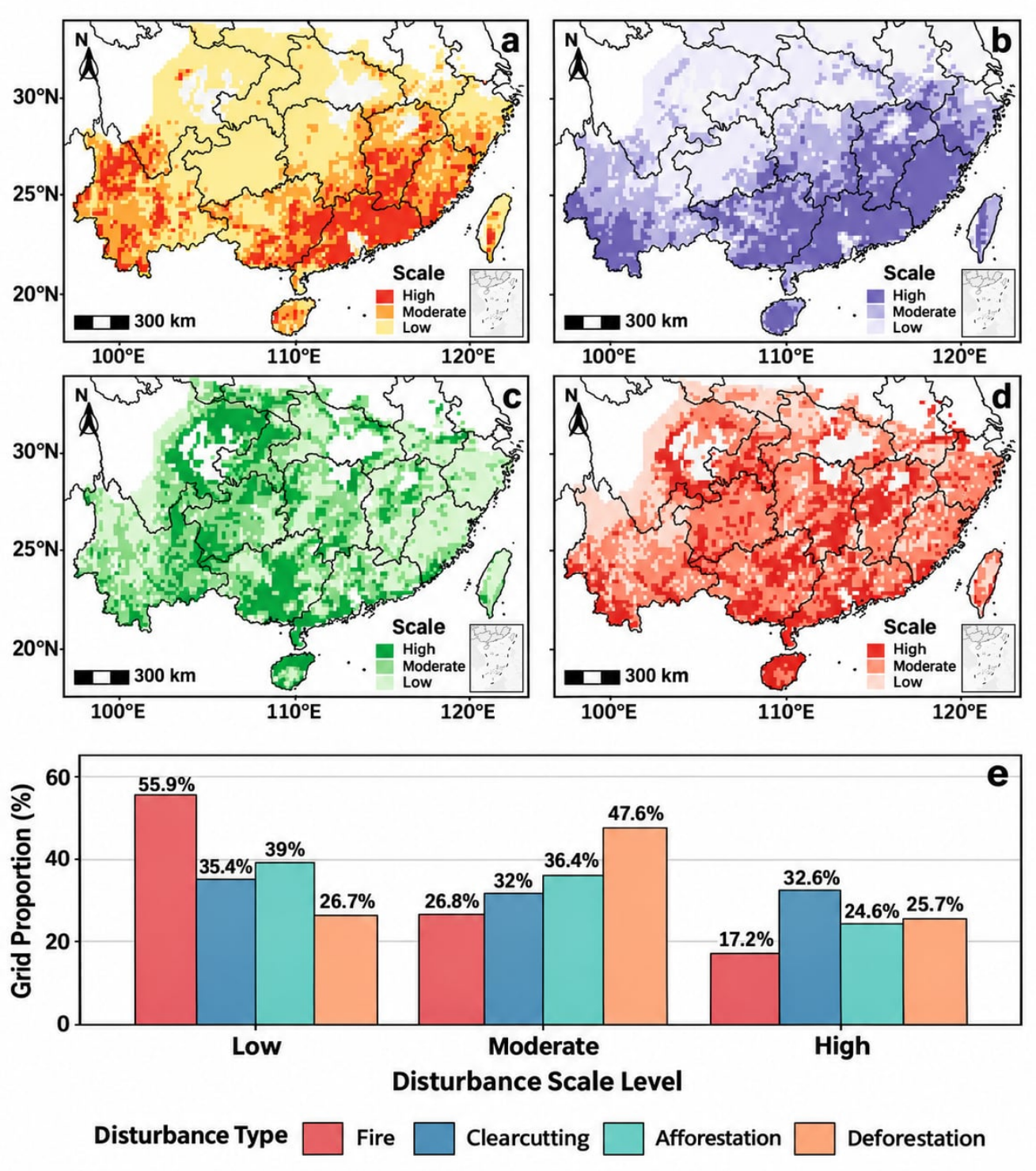

Figure 4. Spatial distribution of change scales (**a**–**d**) and their corresponding grid proportions by scale grades (**e**) for each forest change type during 1993–2021. Panels (**a**–**d**) represent fire, clear-cutting, afforestation, and deforestation, respectively. All spatial statistics and maps in this study are summarized at the 0.2° grid-cell scale, based on the aggregated pixel-level change area for each forest-change type.

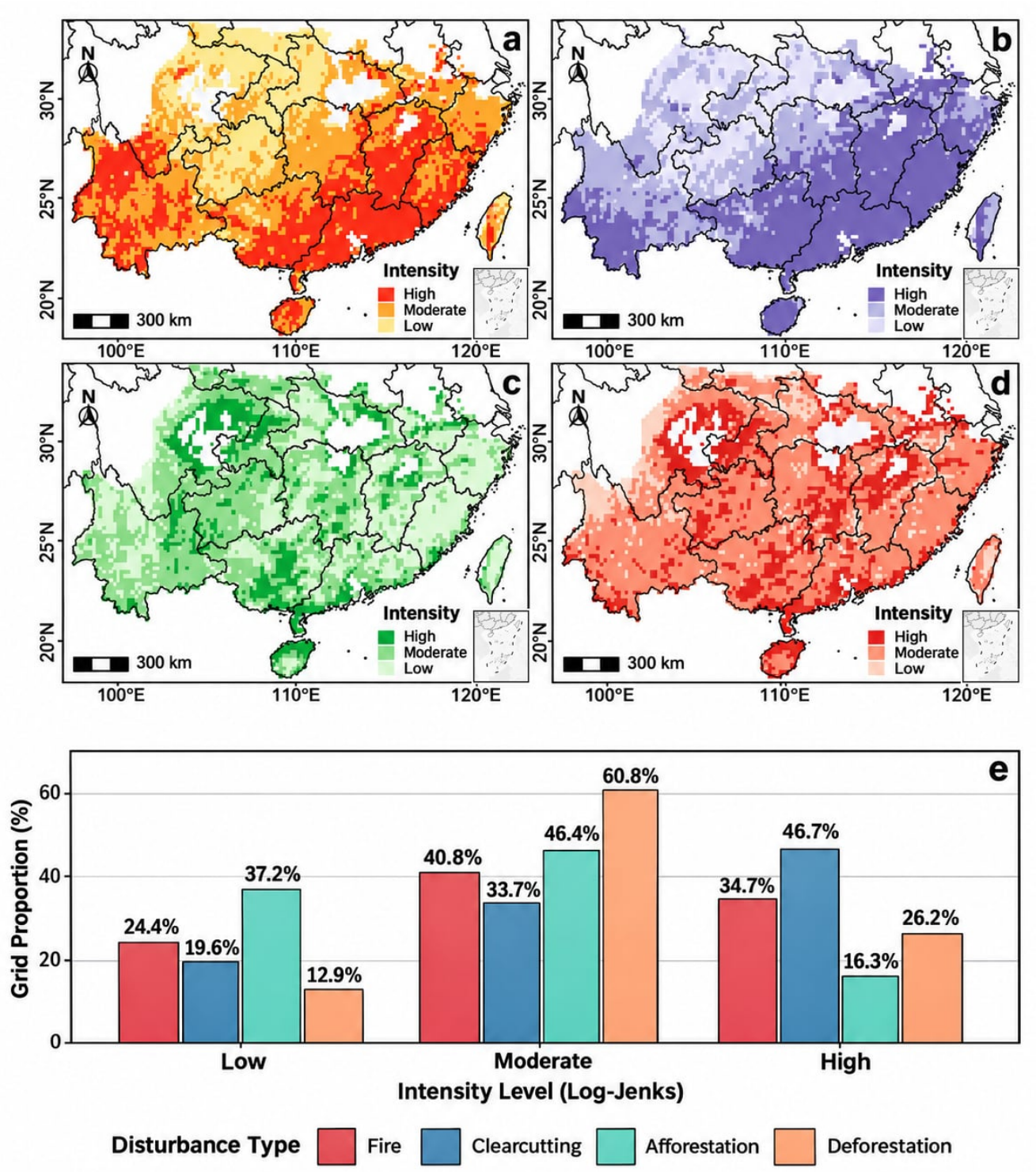

Figure 5. Spatial distribution of period-summary forest-change intensity during 1993–2021 (**a**–**d**) and proportions of analyzed grid cells in each intensity class (**e**). Panels (**a**–**d**) represent fire, clear-cutting, afforestation, and deforestation, respectively. Classes were defined separately for each change type using log-transformation and Jenks natural breaks (Table S2).

3.2.2. Temporal Trends of Forest Change Types

The four forest-change types show distinct distributions of peak-intensity years and temporal trends during 1993–2021 (Figures 6 and 7). Grid-level maximum annual fire intensity occurred most frequently during 2006–2010 and least frequently during 2016–2021; 52.1% of analyzed grids exhibited significant or non-significant decreases. For clear-cutting,

grid-level intensity maxima occurred frequently during 2006–2015, while some southern zones reached their maxima in later years; 28.4% of grids showed significant increases. Grid-level maximum annual afforestation intensity occurred most frequently during 1993–2000, and 48.7% of grids showed significant or non-significant increases over the full period. For deforestation, 44.8% of the grids included in the peak-year analysis reached their maximum annual intensity during 2011–2015. This percentage represents a proportion of grids rather than a share of total deforestation area. Over the full study period, 62.8% of deforestation grids showed significant or non-significant increases.

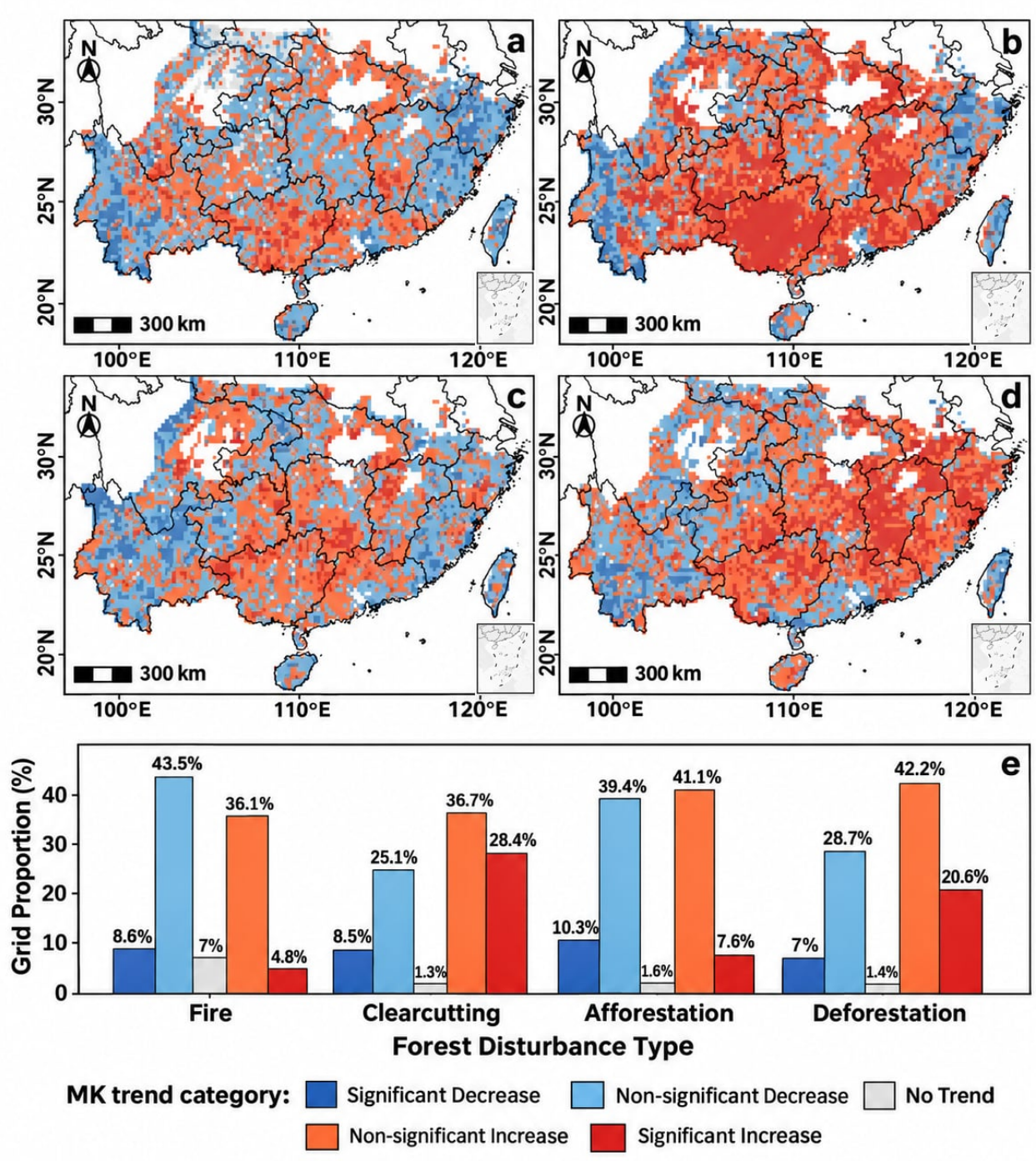

Figure 6. Spatial distribution of Mann–Kendall trends in annual forest-change intensity during 1993–2021 (**a**–**d**) and corresponding grid proportions by trend category (**e**). Panels (**a**–**d**) represent fire, clear-cutting, afforestation, and deforestation, respectively.

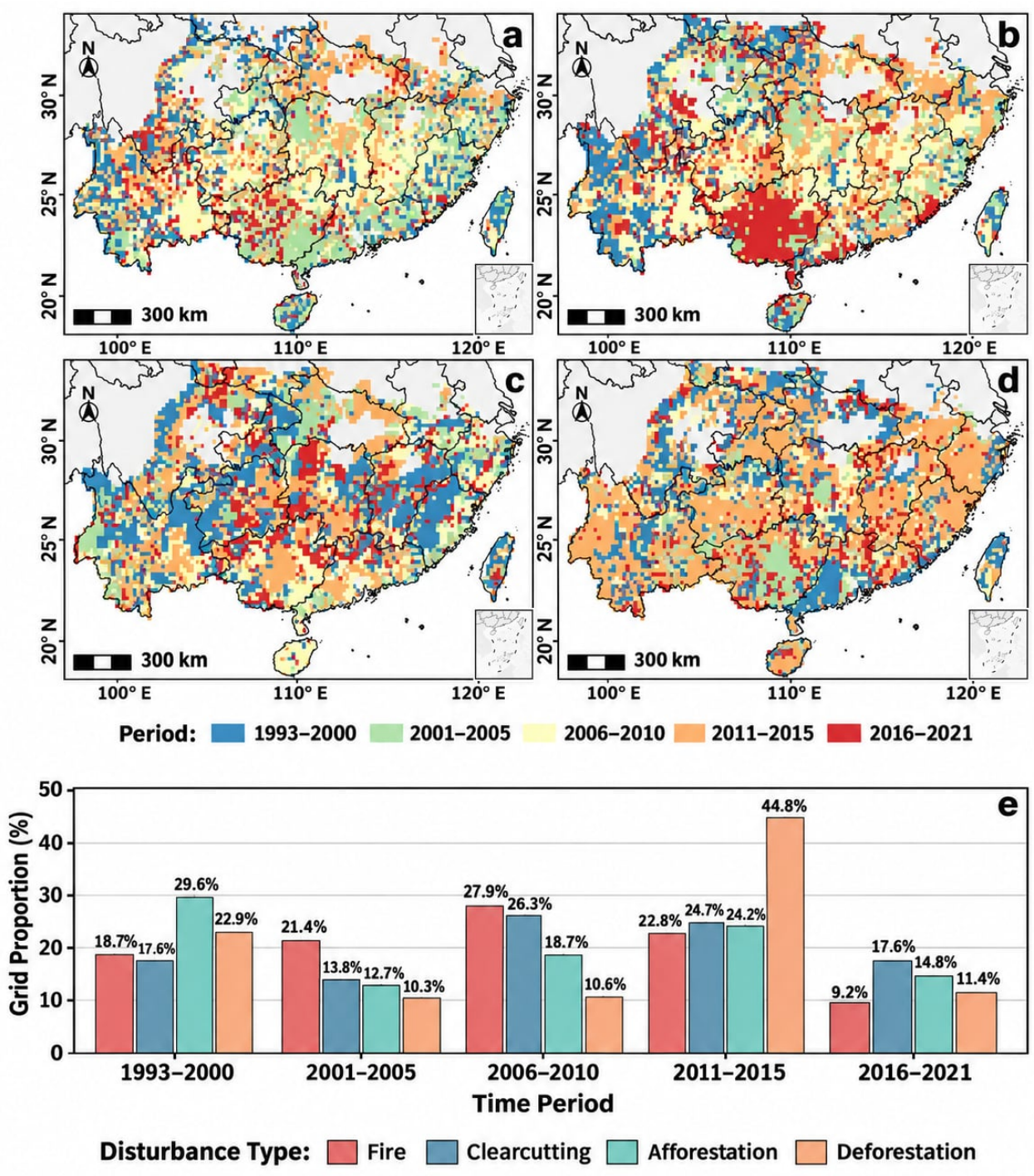

Figure 7. Spatial distribution maps of peak change years (**a**–**d**) and their corresponding grid proportions by peak change year grades (**e**) for each forest change type from 1993 to 2021. Panels (**a**–**d**) represent fire, clear-cutting, afforestation, and deforestation, respectively. Panel (**e**) reports the percentage of included grids whose maximum annual intensity year falls within each interval. The intervals contain 8, 5, 5, 5, and 6 years, respectively.

3.3. Model-Based Analysis of Annual Forest-Change Intensity Classes

3.3.1. Global Feature-Importance Ranking

Table 5 summarizes the performance of the XGBoost models for the four change types. The clear-cutting model performs best, followed by deforestation, whereas afforestation and fire are more challenging to predict—fire showing the lowest OA and Kappa. All models achieve multi-class AUC values above 0.73. As shown in Figure 8, the leading predictors

differ across change types. Potential evapotranspiration, elevation, and mean temperature rank as the top three factors for fire, with high-intensity contributions dominating. Mean temperature and potential evapotranspiration are the leading explanatory covariates associated with clear-cutting patterns, with low-intensity contributions prevailing. Slope makes the largest contribution to the model predictions for both afforestation and deforestation, followed by population size as an important socioeconomic predictor. Topographic and climatic factors dominate the remaining key rankings for both afforestation and deforestation, though with distinct feature-order differences between the two types.

Table 5. Performance of XGBoost classification models for annual forest-change intensity classes.

Type	Overall Accuracy	Kappa	Multi-Class AUC	Macro-F1 Score
Fire	0.5513 ± 0.0024	0.3072 ± 0.0037	0.7343 ± 0.0014	0.5424 ± 0.0026
Clear-cutting	0.6719 ± 0.0029	0.4848 ± 0.0048	0.8386 ± 0.0017	0.6611 ± 0.0031
Afforestation	0.6042 ± 0.0027	0.3682 ± 0.0043	0.7913 ± 0.0016	0.5988 ± 0.0028
Deforestation	0.6294 ± 0.0021	0.4106 ± 0.0032	0.8180 ± 0.0018	0.6311 ± 0.0023

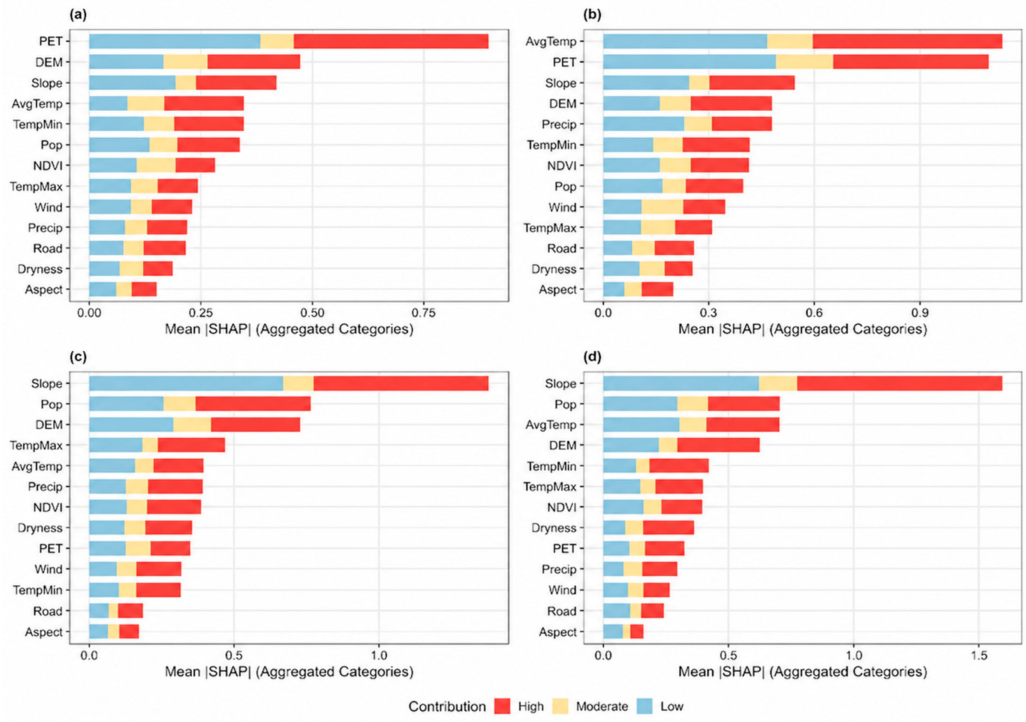

Figure 8. Global SHAP importance for XGBoost models of annual forest-change intensity classes. Panels (**a**–**d**) represent fire, clear-cutting, afforestation, and deforestation, respectively. Colors indicate contributions to the low-, moderate-, and high-intensity class outputs of the annual models.

3.3.2. Nonlinear Associations with the Annual High-Intensity Class Output

For the annual high-intensity class, SHAP dependence plots reveal distinct nonlinear driver–response relationships across the four change types (Figure 9). Topographically, higher slope values generally correspond to lower SHAP contributions to the high-intensity class output, particularly for afforestation and deforestation. Among climatic covariates, potential evapotranspiration was strongly associated with high-intensity fire, whereas mean temperature was an important explanatory covariate for high-intensity clear-cutting. The SHAP contribution of mean temperature changed from negative to positive at particular values in the fitted relationship. Among socioeconomic variables, population density is

an important predictor for both high-intensity afforestation and high-intensity deforestation, with its SHAP contributions generally increasing before plateauing at higher values. These patterns suggest that the fitted relationships between high-intensity forest change and topographic, climatic, and socioeconomic variables are nonlinear. They provide a basis for examining possible environmental and management explanations, although the dependence plots alone do not establish causal interactions or demonstrate the inadequacy of all linear models.

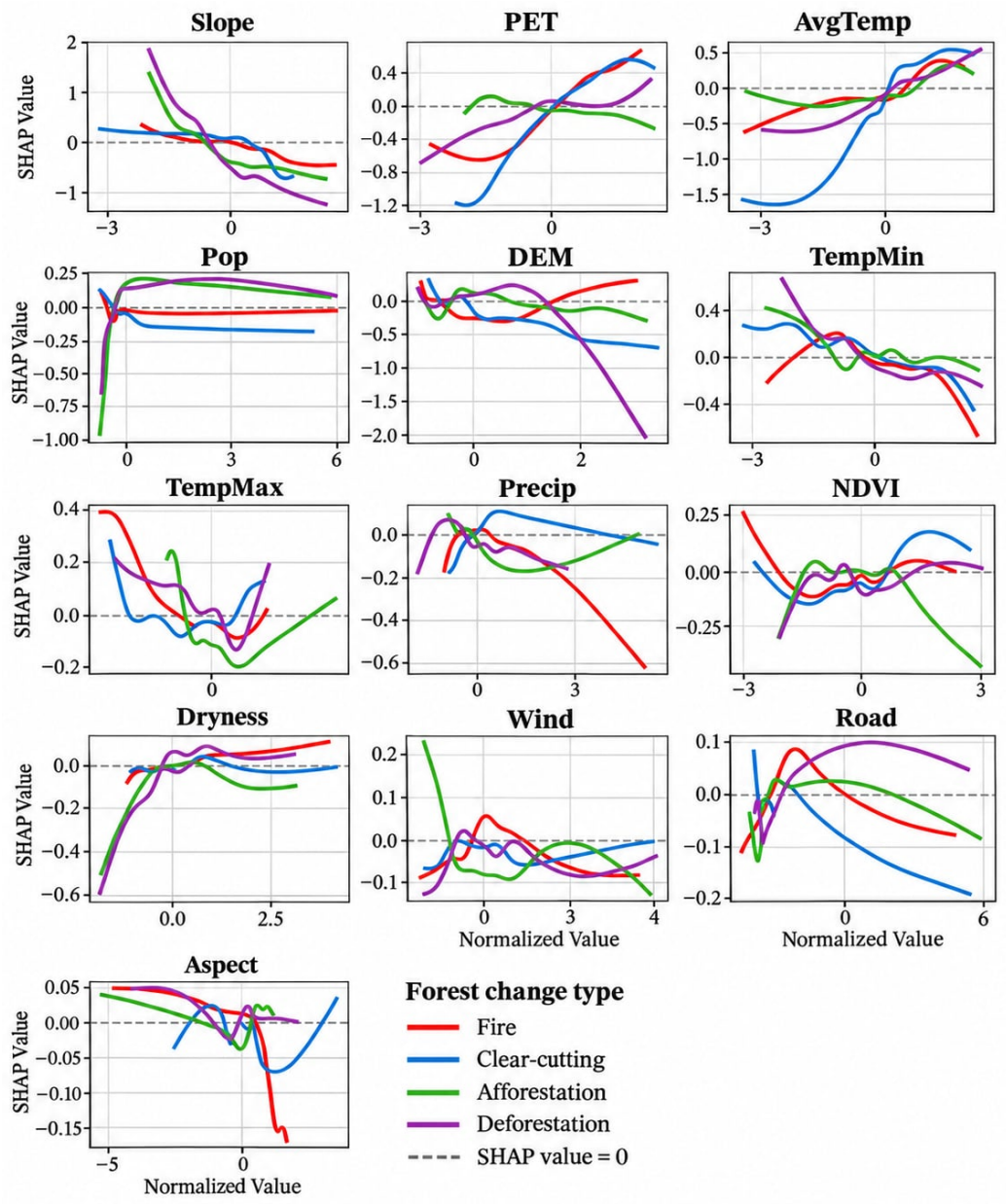

Figure 9. SHAP dependence curves for the annual high-intensity class output of the forest-change models. The *x*-axis shows standardized predictor values (z-scores), and the *y*-axis shows class-specific SHAP contributions relative to the baseline output. Positive and negative values indicate upward and downward contributions to that class output, respectively.

The spatial patterns of dominant positive and negative SHAP contributions exhibit clear differences across forest-change types (Figure 10). Potential evapotranspiration is the dominant positive contributor to the fire-model output in the southeastern and southwestern cores, showing broad spatial correspondence with the period-summary fire pattern described in Section 3.2.1; potential evapotranspiration and elevation are prominent nega-

tive contributors across inland areas. Mean temperature makes both positive and negative contributions to the clear-cutting model. Positive contributions in southern forest zones may reflect the spatial coincidence of favorable hydrothermal conditions, fast-growing plantations, and shorter economic rotations, whereas negative contributions in west-to-central-south regions may be consistent with cooler conditions and slower growth. Spatial differences in the contributions of potential evapotranspiration and minimum temperature suggest variation in the climatic associations represented by the model. Slope makes dominant positive contributions to the afforestation model in inland, coastal, and tropical areas and dominant negative contributions across approximately 60% of the region, with elevation and population also contributing negatively in some areas. For deforestation, slope makes dominant positive contributions in southern coastal and central-eastern zones and dominant negative contributions across approximately 70% of the study area. Elevation makes prominent negative contributions in western high-mountain areas.

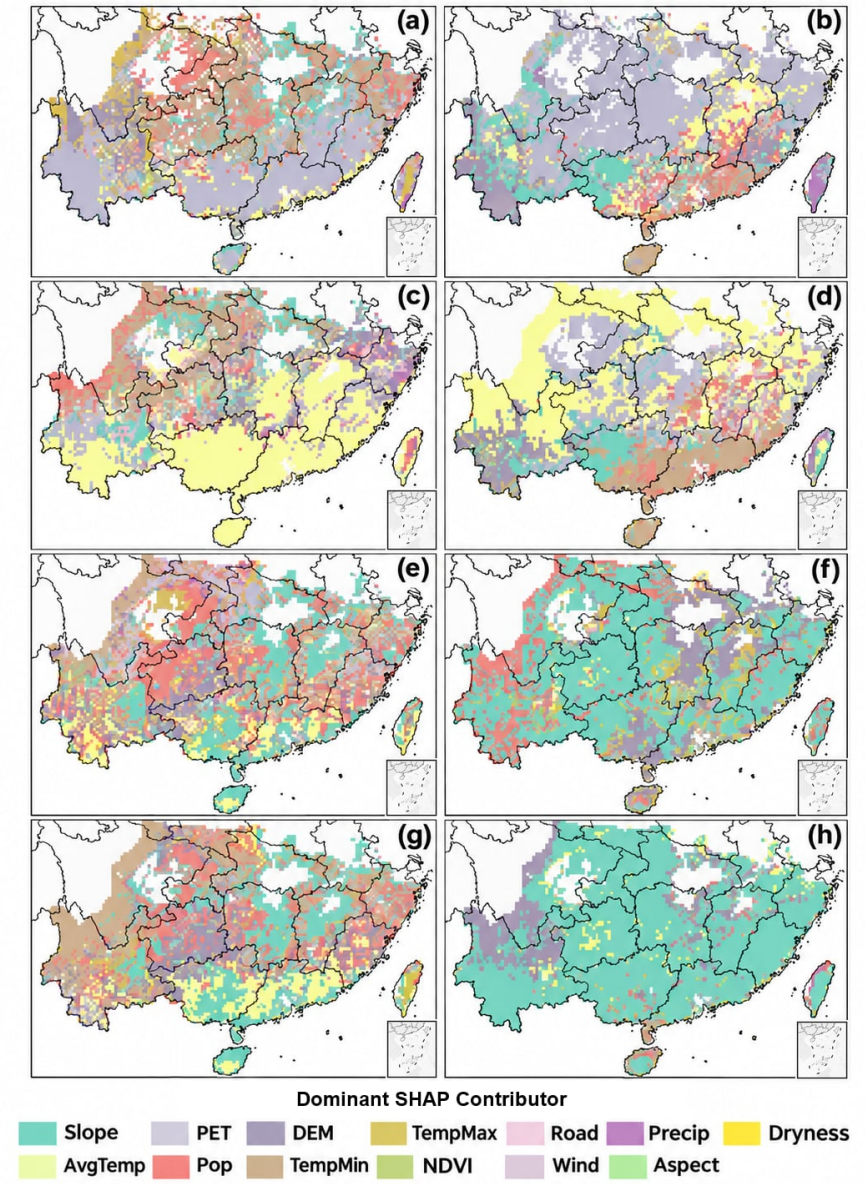

Figure 10. Spatial distribution of dominant positive and negative SHAP contributors to the annual high-intensity class output. Panels (**a**,**b**) represent positive and negative contributors for fire; (**c**,**d**) for clear-cutting; (**e**,**f**) for afforestation; and (**g**,**h**) for deforestation, respectively. Contributions from the annual models are summarized at the 0.2° grid-cell scale.

4. Discussion

4.1. Interpretation of Forest Change Spatiotemporal Patterns

4.1.1. Spatial Aggregation Patterns

The dual-core aggregation pattern shared by fire and clear-cutting represents a central finding of this study and carries important ecological and managerial implications. The southeastern fire core aligns closely with the national-scale wildfire pattern documented by Lian et al. [15], who identified southern and southwestern China as the two most fire-prone regions. The southwestern fire core, located primarily in Yunnan and adjacent border regions, reflects a region of known high fire risk in response to dry-hot valley conditions induced by foehn effects in the Hengduan Mountains [35]. The close congruence between the dual-core aggregation patterns of fire and clear-cutting, despite their distinct underlying mechanisms, underscores the shared sensitivity of both processes to regional hydrothermal conditions and human zoning regimes. However, for clear-cutting, the southeastern core extends over a broader geographic range—a pattern attributable to the expanding fast-growing plantation economy in Guangxi, Guangdong, and Fujian provinces, where short-rotation eucalyptus and pine plantations now dominate the industrial wood supply. The concentration of clear-cutting in Yunnan border regions reflects, in part, the influence of cross-border economic development models and forest management policies, generating sharp clear-cutting intensity gradients between adjacent regions—a finding consistent with earlier sub-national studies [36].

The highly congruent spatial distributions of afforestation and deforestation merit particular attention. Afforestation concentrates in central–southern Guangxi, the Leizhou Peninsula, northern Hainan, the Yunnan–Guizhou border, eastern Sichuan, and the Qinba Mountains. Among these, Guangxi and its surroundings are typical of dense plantation landscapes undergoing cycles of large-scale harvesting and subsequent afforestation; the Yunnan–Guizhou border and parts of Hunan are representative of the Grain for Green Program, featuring large-scale artificial afforestation and restoration forests [8]; and the Sichuan–Chongqing region, Yunnan–Guizhou Plateau, and Qinba Mountains have been verified to harbor substantial afforestation and forest-densification potential [37], rendering them core afforestation zones in the study area. Deforestation shows high spatial similarity to afforestation in the period-summary maps, with more pronounced spatial differentiation. This spatial overlap is compatible with possible loss–recovery or plantation-rotation pathways. However, the period-summary maps alone cannot establish the temporal sequence of these processes or quantify the proportion of compensatory afforestation. These interpretations require validation using linked pixel-level event histories. Compared with global tropical regions (e.g., the Amazon Basin, sub-Saharan Africa, and Southeast Asia), forest changes in China's tropical and subtropical regions display distinct characteristics: global tropical forest changes are more scattered and closely associated with commercial development activities, whereas China's forest changes are concentrated in specific regions and strongly regulated by national and local forest policies—reflecting the distinctive Chinese context of state-led forest management.

4.1.2. Temporal Evolution Trends

The four forest-change types exhibit distinct temporal trajectories, jointly shaped by policy interventions, climate change, and socioeconomic development. Annual fire intensity shows an overall declining trend with localized variation; relatively few grids reached their maximum annual intensity during 2016–2021. This timing pattern is consistent with reduced recent fire activity, although peak-year proportions alone do not quantify regional fire totals or event severity. This temporal trend aligns closely with China's long-term forest fire-prevention and control efforts, including the establishment of a strict fire-prevention

responsibility system and the implementation of the Natural Forest Protection Program (NFPP) since 2000, which have substantially reduced fire risk. Clear-cutting displays a distinct dominant growth trend, with significant increases concentrated in Guangxi, Guizhou, Guangdong, and Jiangxi. In Guangxi, grid-level annual clear-cutting intensity maxima were concentrated during 2016–2021, potentially associated with large-scale eucalyptus planting, short rotation cycles, and rising timber-market demand [38]. In other provinces, peak annual clear-cutting intensity years were concentrated during 2006–2015, potentially associated with salvage logging following the 2008 ice-snow disaster, which caused widespread forest damage [39].

Afforestation has maintained an overall increasing trend across the study period. Since the launch of the NFPP in the late 1990s, China's forest policies have gradually shifted from mountain-closure reforestation and Grain for Green to large-scale national afforestation and forest-quality improvement, delivering remarkable forest restoration outcomes [40].

The concentration of deforestation peaks during 2011–2015 warrants cautious interpretation. Previous research has documented spurious transitions and temporal-consistency issues in CLCD and other annual land-cover products [41]. Differences in product definitions and detection methods also limit direct comparisons, particularly because Hansen GFC measures gross tree-cover loss rather than persistent forest-to-non-forest conversion. Insufficient independent reference data further constrain validation of the observed temporal pattern. Its attribution to forest management or policy changes therefore remains uncertain. Future work will prioritize independent validation of afforestation and deforestation using reference samples interpreted from historical Landsat imagery across different periods, to better assess uncertainties in the detected transitions and their temporal trends.

Compared with global tropical forest changes, the study area exhibits distinct temporal trends. For example, fire severity in global tropical and subtropical ecosystems has increased over the past two decades [42], and forest loss in regions such as the Amazon Basin and Southeast Asia remains severe, with the global net forest-loss rate rebounding during 2015–2025 [43]. The fundamental difference between China and the global trend lies in the strong policy regulation of China's forest changes, which has rendered forest resources recoverable and controllable.

4.2. Factors Associated with Annual Forest-Change Intensity Classes

4.2.1. Dominant Drivers Across Forest-Change Types

The drivers of forest change vary across change types; however, natural disturbance under climate change and socioeconomic factors remain the core forces shaping global forest dynamics. Furthermore, this study contends that topographic factors cannot be overlooked in forest change processes [44]. In China's tropical and subtropical regions, the dominant drivers exhibit clear regional characteristics while remaining consistent with global general trends. For fire, potential evapotranspiration makes the largest positive model contribution in core regions. This association may be consistent with an interpretation involving climatic evaporative demand and fuel-drying conditions under warming [45]; however, potential evapotranspiration is not a direct measure of fuel moisture, and this pathway was not independently tested in the present study. In parts of northern Yunnan, elevation is the leading positive SHAP contributor. This pattern may reflect topographic and climatic conditions associated with the dry-hot valleys of the Hengduan Mountains, where foehn effects have been discussed in relation to fire-prone conditions [35].

Mean temperature should not be interpreted as a direct physical cause of clear-cutting. Rather, it is an environmental covariate associated with plantation productivity, species suitability, and rotation intensity. Warmer areas in southern China often coincide with fast-growing plantation systems, where higher productivity may support shorter harvest

cycles. The AvgTemp SHAP signal therefore likely captures climatic suitability together with spatial confounding from plantation distribution and management intensity. Minimum temperature may additionally reflect exposure to cold events associated with salvage logging [46], consistent with the broader relationship between climate variability, extreme weather, and salvage harvesting reported by [47].

In the annual intensity-class models, slope is a leading predictor for afforestation and deforestation. CLCD-based statistics indicate that most mapped afforestation transitions originate from cropland, a pattern consistent with the possible influence of the Grain for Green Program [48], while most mapped deforestation transitions end in cropland, which may be associated with agricultural expansion. In Guizhou, eastern Sichuan, and the Qinba Mountains, population size is the leading positive SHAP contributor to the afforestation model, suggesting an association with the spatial distribution of human activities and forest-restoration initiatives [49]. Mean temperature also makes positive contributions to the deforestation-model output in some settings. Mao et al. [50] reported greater warming in areas with declining forest cover than in areas with increasing cover, providing relevant context for this association without establishing its causal direction.

4.2.2. Nonlinear Model Responses for the Annual High-Intensity Class

Beyond global and regional feature rankings, SHAP analysis of the annual high-intensity class identifies differences among the nonlinear fitted relationships and their spatial patterns. In the SHAP dependence plots, higher slope values generally correspond to lower contributions to the high-intensity class output, particularly for afforestation and deforestation, while elevation is an important predictor for deforestation. Among climatic variables, potential evapotranspiration makes positive contributions to the high-intensity fire and clear-cutting outputs in parts of the fitted relationships, while the mean-temperature signal for clear-cutting may reflect plantation productivity, suitability, and rotation conditions. Population density is an important predictor for both high-intensity afforestation and deforestation. These associations provide useful context for regional management and generate hypotheses about underlying processes.

The spatial patterns of dominant positive and negative SHAP contributors to the annual high-intensity class output provide additional information on regional variation in the fitted relationships. Potential evapotranspiration makes dominant positive contributions to the fire-model output in the southeastern and south-western cores, showing broad spatial correspondence with the period-summary fire distribution discussed in Section 4.1.1. A possible interpretation involves the relationship between climatic evaporative demand and fuel-drying conditions, although potential evapotranspiration alone cannot establish fuel dryness or ignition processes. Across inland areas, potential evapotranspiration and elevation are prominent negative contributors to the fire-model output, which may reflect different combinations of environmental conditions represented in the training data. Mean temperature is a leading environmental covariate in the clear-cutting model: positive contributions in southern forest zones may reflect the coincidence of favorable hydrothermal conditions, fast-growing plantations, and shorter rotations, while negative contributions in west-to-central-south regions may be consistent with cooler conditions and slower growth. These interpretations are compatible with the southern concentration and short-rotation management discussed for the study area, but the SHAP patterns alone do not establish harvesting or recovery mechanisms. Differences in the spatial contributions of potential evapotranspiration and minimum temperature further suggest variation in the climatic and management contexts represented by the model.

For afforestation and deforestation, slope is a dominant positive contributor in some locations and a dominant negative contributor in others. The rugged terrain of tropical and

subtropical China provides a plausible context: steep slopes (>25°) can present erosion risks and limit activities such as planting, harvesting, and infrastructure construction. Slope was identified as the dominant negative SHAP contributor across approximately 60–70% of the spatial summaries for afforestation and deforestation, respectively. This pattern may be related to accessibility, land suitability, and policies such as the Regulations on the Conversion of Cropland to Forests Program, although their individual contributions were not separately estimated. Negative elevation contributions in western high-mountain areas may similarly reflect limited accessibility, agricultural suitability, and human activity. Population density makes both positive and negative contributions to the model outputs, potentially reflecting competing land uses in populated areas. Afforestation initiatives, including Grain for Green and timber-based projects, may coexist with demand for agricultural and construction land. These interpretations suggest that institutional and market conditions may both be relevant, rather than demonstrating a causal effect of population density or the independent role of institutional regulation.

The fitted associations may be interpreted in the context of regional differences in forest management, policy, and environmental conditions. First, a fundamental difference exists in post-clear-cutting land use and resilience. Global tropical clear-cutting is frequently accompanied by permanent conversion to plantations (e.g., oil palm, soybean), leading to irreversible forest loss [51]. In contrast, clear-cutting in the study area—especially in eucalyptus-producing provinces like Guangxi, Guangdong, and Fujian—mostly involves short-rotation cycles (5–7 years), with rapid recovery via coppicing or replanting, exhibiting policy-regulated recoverability. This is supported by China's Collective Forest Tenure Reform (since 2003) and the development of fast-growing timber bases. The spatial variation in the SHAP contributions of temperature and potential evapotranspiration may be consistent with this growth–rotation context, although the model does not independently identify the management processes responsible. Second, the role of national intervention differs significantly. Administrative enforcement and sustained fiscal investment provide a possible policy context for the observed forest-change patterns in China, including variation in the timing of changes. Their independent effects on fire, clear-cutting, afforestation, and deforestation were not estimated in the present models. In contrast, global tropical forest changes are more heavily driven by economic factors (e.g., agricultural expansion) and climate anomalies [42]; thus, the relevance of Chinese management practices elsewhere should be considered in light of socioeconomic and institutional differences. Third, the hydrothermal conditions of tropical and subtropical China may support forest recovery and help explain the climatic associations represented by the models, including the positive mean-temperature contributions to clear-cutting predictions in southern areas. Recovery outcomes and the persistence of forest conversion nevertheless require evidence beyond the SHAP analysis.

4.2.3. Potential Cascading and Coupled Change Processes

Potential cascading and coupled processes also qualify the interpretation of the four mapped types. The strong spatial congruence between afforestation and deforestation suggests that some locations may pass through sequential loss-and-recovery pathways rather than represent independent gains and losses. In short-rotation plantation regions such as Guangxi, Guangdong, and Fujian, clear-cutting may be followed by coppice recovery or replanting, so a clear-cutting–afforestation sequence can represent one management cycle rather than net forest expansion. Fire may similarly precede either persistent conversion or recovery: canopy removal and post-fire access can increase the opportunity for subsequent land conversion, whereas restoration can produce a later afforestation signal. Conversely, pre-existing harvesting and fragmented stands may alter fuel continuity and fire susceptibil-

ity. Because the present fusion assigns one priority-based label to same-year overlaps and suppresses repeated signals within a three-year window, the maps quantify the dominant recorded transition rather than the complete event cascade. Future analyses should link pixel-level event histories through transition matrices, lagged conditional probabilities, or multi-state models to distinguish rotation cycles, disturbance-driven conversion, and recovery pathways.

4.3. Limitations and Future Research Directions

Despite a relatively comprehensive investigation of forest changes in China's tropical and subtropical regions, this study has several limitations. First, limited data availability prevented us from including several potentially relevant socioeconomic factors in the models, including forest ownership, the intensity of tenure reform, timber prices, and market demand. Previous studies in China have found that the devolution of collective forest rights to households was associated with an increase in the area planted with trees [52] and that timber supply responded to timber prices shaped by market supply and demand [53]. If the omitted factors are correlated with population density or road-network density, the SHAP contributions of these predictors may partly reflect differences in local forest tenure or timber market conditions. The use of a single 2018 road layer also introduces temporal mismatch, particularly for earlier years, and may bias road-related associations. This static proxy cannot capture road expansion or reconstruct accessibility at the time of individual forest-change observations; its model contribution should therefore not be interpreted as the effect of contemporaneous road development. Second, the 0.2° spatial resolution adopted has inherent limitations in capturing micro-scale forest-change features (e.g., small-scale clear-cutting or localized fire events), potentially affecting the granularity of spatial pattern analysis. Third, although the four forest-change types are integrated into the spatiotemporal and driver analysis frameworks, the current study still lacks in-depth coupled analysis of interactions between multiple change types (e.g., the link between clear-cutting and subsequent afforestation, or the feedback loop between fire and deforestation), hindering deeper understanding of the intrinsic mechanisms governing forest-system change. Fourth, the lack of independent validation for afforestation and deforestation introduces some uncertainty into their spatial patterns and temporal trends, while the limited predictive accuracy of the machine-learning models, particularly the fire model (Table 5), adds uncertainty to the SHAP-based interpretations. The identified associations remain informative, while detailed local attributions require caution.

Future research can be expanded in four directions to address these gaps. (i) Integrate multi-source socioeconomic data—including policy documents, market-price data, and rural survey data—to deepen comprehensive exploration of the driving mechanisms of forest change and clarify the complex interactions between socioeconomic factors and ecological processes. Future work should incorporate historical road-network data to improve temporal alignment and assess the sensitivity of road-related associations to this static approximation. (ii) Improve spatial resolution via high-resolution remote-sensing data to achieve finer-scale characterization, strengthen the capture of spatial heterogeneity in forest change, and reduce potential biases caused by scale effects. (iii) Conduct in-depth analysis of interactions between multiple forest-change types, establish coupled models of forest change, and systematically explore the deep intrinsic mechanisms and feedback effects of forest-system change, thereby providing more scientific and targeted support for regional forest resource management and ecological protection. (iv) Independently validate afforestation and deforestation data using historical reference samples, and assess class-specific model performance and SHAP stability through spatially independent validation to strengthen confidence in model interpretation.

5. Conclusions

This study provides a systematic investigation of the spatiotemporal patterns and dominant drivers of four major forest-change types—fire, clear-cutting, afforestation, and deforestation—in China's tropical and subtropical regions, integrating a multi-source remote-sensing dataset (1993–2021) and a unified XGBoost–SHAP analytical framework. The period-summary maps show that fire and clear-cutting exhibit a southeast–southwest dual-core aggregation pattern, whereas afforestation and deforestation show highly congruent and largely dispersed distributions dominated by the moderate period-summary intensity class. Temporally, fire showed decreasing trends in 52.1% of grids, while clear-cutting showed significant increases in 28.4% of grids and afforestation showed increases in 48.7% of grids. For deforestation, 44.8% of the grids included in the peak-year analysis reached their maximum annual intensity during 2011–2015, although this concentration may partly reflect temporal inconsistencies in the underlying CLCD data. In the annual intensity models, potential evapotranspiration is a dominant meteorological factor associated with fire, whereas mean temperature is a leading environmental covariate associated with clear-cutting; the latter likely represents climatic suitability and plantation rotation conditions rather than a direct physical cause. Slope and population are important predictors for afforestation and deforestation. In the spatial summaries of SHAP contributions to the annual high-intensity class output, slope is a prominent negative contributor, particularly for afforestation and deforestation. Post-clear-cutting land use in managed plantation areas may involve short-rotation cycles and recovery rather than permanent conversion.

These findings improve understanding of subtropical forest dynamics through a framework that integrates multi-type forest-change mapping with model-based interpretation of annual intensity classes and nonlinear associations with the annual high-intensity class output. The period-summary maps characterize long-term spatial patterns, while the annual intensity-class models provide complementary information on associations with environmental and socioeconomic variables. These results can inform regional forest management, climate-adaptive silviculture, and ecological policy design. Future work should refine spatial resolution, incorporate dynamic policy variables, and establish coupled models between change types to examine forest-system feedbacks.

Supplementary Materials: The following supporting information can be downloaded at https://www.mdpi.com/article/10.3390/rs18223949/s1: Table S1: Pixel-year overlap statistics among CLCD-derived afforestation and deforestation and CCDC-detected fire and clear-cutting, 1993–2021; Table S2: Class boundaries for the period-summary forest-change intensity maps at the 0.2° grid-cell scale during 1993–2021; Table S3: Annual proportions of post-deforestation land-use transition destinations derived from CLCD data, 1993–2021.

Author Contributions: Conceptualization, Y.W., M.Z. and D.L. (Dengqiu Li); methodology, Y.W. and D.L. (Dengqiu Li); software, Y.W. and M.Z.; validation, Y.W. and M.Z.; formal analysis, Y.W.; investigation, Y.W.; resources, Z.W. and P.H.; data curation, Y.W.; writing—original draft preparation, Y.W.; writing—review and editing, D.L. (Dengqiu Li) and D.L. (Dengsheng Lu); visualization, Y.W.; supervision, D.L. (Dengqiu Li) and D.L. (Dengsheng Lu); funding acquisition, D.L. (Dengqiu Li). All authors have read and agreed to the published version of the manuscript.

Funding: This work was supported by the National Natural Science Foundation of China (32371865), the National Key R&D Program of China under Grants (2021YFD220040102), and the Forestry Science and Technology Projects of Fujian Provincial Forestry Bureau (2026FKJ29).

Data Availability Statement: The data that support the findings of this study are openly available in [GEE] at (https://code.earthengine.google.com/?asset=projects/ee-zhoumingxing993/assets/SubT_SR_2000_2020 (accessed on 7 October 2026)).

Conflicts of Interest: The authors declare no conflicts of interest.

Abbreviations

The following abbreviations are used in this manuscript:

AUC	Area Under the Curve
AVHRR	Advanced Very-High-Resolution Radiometer
CCDC	Continuous Change Detection and Classification
CFTR	Collective Forest Tenure Reform
FAO	Food and Agriculture Organization of the United Nations
FireCCI51	Fire Climate Change Initiative, version 5.1
GEE	Google Earth Engine
GRIP4	Global Roads Inventory Project, version 4
MK	Mann–Kendall
MMU	Minimum Mapping Unit
MODIS	Moderate Resolution Imaging Spectroradiometer
NBR	Normalized Burn Ratio
NDVI	Normalized Difference Vegetation Index
NFPP	Natural Forest Protection Program
NIR	Near-Infrared
OA	Overall Accuracy
PA	Producer's Accuracy
SRF	Spatial Random Forest
SHAP	SHapley Additive exPlanations
SWIR1	Short-Wave Infrared 1
UA	User's Accuracy
WGS84	World Geodetic System 1984
XGBoost	eXtreme Gradient Boosting

References

1. Hansen, M.C.; Potapov, P.V.; Moore, R.; Hancher, M.; Turubanova, S.A.; Tyukavina, A.; Thau, D.; Stehman, S.V.; Goetz, S.J.; Loveland, T.R.; et al. High-resolution global maps of 21st-century forest cover change. *Science* **2013**, *342*, 850–853. [CrossRef]
2. Millennium Ecosystem Assessment. *Ecosystems and Human Well-Being: Wetlands and Water*; World Resources Institute: Washington, DC, USA, 2005.
3. Myers, N. *The Primary Source: Tropical Forests & Our Future*; W. W. Norton & Company: New York, NY, USA, 1992; p. xxxii-416. Available online: https://www.cabidigitallibrary.org/doi/full/10.5555/19920661903 (accessed on 25 July 2025).
4. Wijenayake, P.R.; Shitara, T.; Hirata, A.; Matsui, T.; Kubota, Y.; Masaki, T. Changes in forest ecosystem stability under climate change in a temperate landscape. *Front. For. Glob. Change* **2025**, *7*, 1501987. [CrossRef]
5. Jolly, W.M.; Cochrane, M.A.; Freeborn, P.H.; Holden, Z.A.; Brown, T.J.; Williamson, G.J.; Bowman, D.M. Climate-induced variations in global wildfire danger from 1979 to 2013. *Nat. Commun.* **2015**, *6*, 7537. [CrossRef]
6. Seidl, R.; Thom, D.; Kautz, M.; Martin-Benito, D.; Peltoniemi, M.; Vacchiano, G.; Wild, J.; Ascoli, D.; Petr, M.; Honkaniemi, J.; et al. Forest disturbances under climate change. *Nat. Clim. Change* **2017**, *7*, 395–402. [CrossRef]
7. Chen, C.; Park, T.; Wang, X.; Piao, S.; Xu, B.; Chaturvedi, R.K.; Fuchs, R.; Brovkin, V.; Ciais, P.; Fensholt, R.; et al. China and India lead in greening of the world through land-use management. *Nat. Sustain.* **2019**, *2*, 122–129. [CrossRef]
8. Tong, X.; Brandt, M.; Yue, Y.; Ciais, P.; Rudbeck Jepsen, M.; Penuelas, J.; Wigneron, J.-P.; Xiao, X.; Song, X.-P.; Horion, S.; et al. Forest management in southern China generates short term extensive carbon sequestration. *Nat. Commun.* **2020**, *11*, 129. [CrossRef]
9. Bourgoin, C.; Ceccherini, G.; Girardello, M.; Vancutsem, C.; Avitabile, V.; Beck, P.S.A.; Beuchle, R.; Blanc, L.; Duveiller, G.; Migliavacca, M.; et al. Human degradation of tropical moist forests is greater than previously estimated. *Nature* **2024**, *631*, 570–576. [CrossRef]
10. Sun, J.; Li, G.; Wang, Q.; Zhang, B. Ecological environments of tropical and subtropical regions in China. *Trop. Conserv. Sci.* **2020**, *13*, 1940082920942022. [CrossRef]
11. Yang, J.; Huang, X. The 30 m annual land cover dataset and its dynamics in China from 1990 to 2019. *Earth Syst. Sci. Data* **2021**, *13*, 3907–3925. [CrossRef]
12. Yang, J.; Xu, Y.; Chai, Y.; Cheng, X.; Wu, H.; He, J.; Wu, Y.; Chen, Z.; Ni, Z.; Shi, Y. Mechanisms, processes, and climate change responses of carbon cycling in Chinese subtropical forest ecosystems. *Forests* **2026**, *17*, 330. [CrossRef]
13. Guo, F.; Su, Z.; Wang, G.; Sun, L.; Tigabu, M.; Yang, X.; Hu, H. Understanding fire drivers and relative impacts in different Chinese forest ecosystems. *Sci. Total Environ.* **2017**, *605*, 411–425. [CrossRef]
14. Su, Z.; Tigabu, M.; Cao, Q.; Wang, G.; Hu, H.; Guo, F. Comparative analysis of spatial variation in forest fire drivers between boreal and subtropical ecosystems in China. *For. Ecol. Manag.* **2019**, *454*, 117669. [CrossRef]

15. Lian, C.; Xiao, C.; Feng, Z.; Ma, Q. Accelerating decline of wildfires in China in the 21st century. *Front. For. Glob. Change* **2024**, *6*, 1252587. [CrossRef]
16. Zhou, M.; Li, G.; Lu, D.; Xu, C.; Li, Z.; Li, D. Spatiotemporal patterns of annual clear-cutting distribution in tropical and subtropical regions of China with time series Landsat and CCDC. *Geo-Spat. Inf. Sci.* **2025**, *28*, 2763–2780. [CrossRef]
17. Bi, C.; Yang, K.; Zhang, S.; Zeng, W.; Liu, J.; Rao, Y.; Ma, Y.; Yang, X. Simulation and analysis of afforestation potential areas under different development scenarios in Yunnan Province, China. *Ecol. Indic.* **2024**, *167*, 112695. [CrossRef]
18. Lim, C.L.; Prescott, G.W.; De Alban, J.D.T.; Ziegler, A.D.; Webb, E.L. Untangling the proximate causes and underlying drivers of deforestation and forest degradation in Myanmar. *Conserv. Biol.* **2017**, *31*, 1362–1372. [CrossRef]
19. Zhang, L.; Wang, H.; Wang, Y.; Ding, J.; Shen, J.; Wang, Z.; Liu, Y.; Liang, C.; Li, S. Reconstructing deforestation patterns in China from 2000 to 2019. *Ecol. Model.* **2022**, *465*, 109874. [CrossRef]
20. Reichstein, M.; Camps-Valls, G.; Stevens, B.; Jung, M.; Denzler, J.; Carvalhais, N.; Prabhat, F. Deep learning and process understanding for data-driven Earth system science. *Nature* **2019**, *566*, 195–204. [CrossRef]
21. Georganos, S.; Grippa, T.; Niang Gadiaga, A.; Linard, C.; Lennert, M.; Vanhuysse, S.; Mboga, N.; Wolff, E.; Kalogirou, S. Geographical random forests: A spatial extension of the random forest algorithm to address spatial heterogeneity in remote sensing and population modelling. *Geocarto Int.* **2021**, *36*, 121–136. [CrossRef]
22. Arrogante-Funes, P.; Arrogante-Funes, F.; Feijoo, D.O.; Alvarez-Ripado, A.; Novillo, C.J.; Bruzón, A.G. Exploring spatiotemporal dynamics and drivers of forest ecosystems in southern Europe with explainable machine learning. *Ecol. Inform.* **2025**, *90*, 103343. [CrossRef]
23. Zhang, B.; Ye, S.; Wang, W.; Huang, F.; He, Y. Climate drives environmental efficiency across Chinese provinces. *Trop. Conserv. Sci.* **2019**, *12*, 1940082919873268. [CrossRef]
24. Zhang, X.; Zhao, T.; Xu, H.; Liu, W.; Wang, J.; Chen, X.; Liu, L. GLC_FCS30D: The first global 30 m land-cover dynamics monitoring product with a fine classification system for the period from 1985 to 2022 generated using dense-time-series Landsat imagery and the continuous change-detection method. *Earth Syst. Sci. Data* **2024**, *16*, 1353–1381. [CrossRef]
25. Ding, Y.X.; Peng, S.Z. Spatiotemporal change and attribution of potential evapotranspiration over China from 1901 to 2100. *Theor. Appl. Climatol.* **2021**, *145*, 215–228. [CrossRef]
26. Peng, S.; Ding, Y.; Liu, W.; Li, Z. 1 km monthly temperature and precipitation dataset for China from 1901 to 2017. *Earth Syst. Sci. Data* **2019**, *11*, 1931–1946. [CrossRef]
27. Muñoz-Sabater, J.; Dutra, E.; Agustí-Panareda, A.; Albergel, C.; Arduini, G.; Balsamo, G.; Boussetta, S.; Choulga, M.; Harrigan, S.; Hersbach, H.; et al. ERA5-Land: A state-of-the-art global land surface reanalysis dataset. *Earth Syst. Sci. Data* **2021**, *13*, 4349–4383. [CrossRef]
28. Vermote, E.; NOAA CDR Program. *NOAA Climate Data Record (CDR) of AVHRR Normalized Difference Vegetation Index (NDVI), Version 5*; NOAA National Centers for Environmental Information: Asheville, NC, USA, 2026. [CrossRef]
29. Meijer, J.R.; Huijbregts, M.A.J.; Schotten, C.G.J.; Schipper, A.M. Global patterns of current and future road infrastructure. *Environ. Res. Lett.* **2018**, *13*, 064006. [CrossRef]
30. Liu, X.; State Key Laboratory of Remote Sensing Science; Beijing Normal University. A global gridded population dataset generated by cluster analysis and statistical learning. *Sci. Data* **2024**, *11*, 124. [CrossRef]
31. Tai, Z.; Su, X.; Shen, W.; Wang, T.; Gu, C.; He, J.; Huang, C. Identification of spatial distribution of afforestation, reforestation, and deforestation and their impacts on local land surface temperature in Yangtze River Delta and Pearl River Delta urban agglomerations of China. *Remote Sens.* **2024**, *16*, 3528. [CrossRef]
32. Chen, T.; Guestrin, C. Xgboost: A scalable tree boosting system. In Proceedings of the 22nd ACM SIGKDD International Conference on Knowledge Discovery and Data Mining, San Francisco, CA, USA, 13–17 August 2016; pp. 785–794. [CrossRef]
33. Lundberg, S.M.; Lee, S.I. A unified approach to interpreting model predictions. In Proceedings of the Advances in Neural Information Processing Systems 30, Long Beach, CA, USA, 4–9 December 2017. [CrossRef]
34. Shen, J.; Chen, G.; Hua, J.; Huang, S.; Ma, J. Contrasting forest loss and gain patterns in subtropical China detected using an integrated LandTrendr and machine-learning method. *Remote Sens.* **2022**, *14*, 3238. [CrossRef]
35. Deng, H.; Li, D.; Cai, S.; Zhao, F.; Zhao, J. Spatio-temporal dynamics of forest fire occurrence in Yunnan, China from 2001 to 2021 based on MODIS. *npj Nat. Hazards* **2025**, *2*, 52. [CrossRef]
36. Wang, H.; Bai, Y.; Liu, C.; Huang, L.; Wang, B.; Zhao, Z.; Li, Q.; Chen, D.; Zhang, Z. Spatiotemporal patterns of forest fragmentation along the border region of Yunnan Province in Southwest China from 1985 to 2022. *Glob. Ecol. Conserv.* **2026**, *65*, e04039. [CrossRef]
37. Yao, L.; Liu, T.; Qin, J.; Jiang, H.; Yang, L.; Smith, P.; Chen, X.; Zhou, C.; Piao, S. Carbon sequestration potential of tree planting in China. *Nat. Commun.* **2024**, *15*, 8398. [CrossRef]
38. Yang, Y.; Cai, W.H.; Huang, Q.; Yu, L.; Zu, J.; Wang, J.; Yang, J. Monitoring spatiotemporal expansion dynamics of short-rotation Eucalyptus plantations over large scales using Landsat time-series data. *IEEE J. Sel. Top. Appl. Earth Obs. Remote Sens.* **2024**, *17*, 18915–18925. [CrossRef]

39. Zhou, B.; Wang, X.; Cao, Y.; Ge, X.; Gu, L.; Meng, J. Damage assessment to subtropical forests following the 2008 Chinese ice storm. *iForest-Biogeosci. For.* **2017**, *10*, 406. [CrossRef]
40. National Forestry and Grassland Administration. *China Forest Resources Report (2014—2018)*; China Forestry Publishing House: Beijing, China, 2019. Available online: https://books.google.com/books?id=bbyzDwAAQBAJ (accessed on 7 October 2026).
41. Li, B.; Liu, X.; Zhuang, H.; Shi, Q.; Zeng, L.; Cai, Y.; Zhang, H.; Cai, Y.; Wu, C.; Xu, X. ALCC: Temporally Consistent Annual Land Cover Maps over China from 1985 to 2022 Based on an Ensemble Change Detection Method. *J. Remote Sens.* **2026**, *6*, 1029. [CrossRef]
42. He, K.; Shen, X.; Anagnostou, E. Global burn severity in forest ecoregions: Trends, climate drivers, and predictive insights. *npj Nat. Hazards* **2025**, *2*, 61. [CrossRef]
43. FAO. *Global Forest Resources Assessment 2025*; Food and Agriculture Organization of the United Nations: Rome, Italy, 2025.
44. Ma, J.; Li, J.; Wu, W.; Liu, J. Global forest fragmentation change from 2000 to 2020. *Nat. Commun.* **2023**, *14*, 3752. [CrossRef]
45. Gong, D.; Jing, M. Spatiotemporal dynamics of forest fire risk in southeastern China under climate change: Hydrothermal drivers and future projections. *Atmosphere* **2025**, *16*, 1189. [CrossRef]
46. Zhu, Y.; Liu, S.; Yan, W.; Deng, D.; Zhou, G.; Zhao, M.; Gao, F.; Zhu, L.; Wang, Z.; Xie, M. Impact of ice-storms and subsequent salvage logging on the productivity of Cunninghamia lanceolata (Chinese Fir) forests. *Forests* **2022**, *13*, 296. [CrossRef]
47. Šimůnek, V.; Vacek, Z.; Vacek, S. Solar cycles in salvage logging: National data from the Czech Republic confirm significant correlation. *Forests* **2020**, *11*, 973. [CrossRef]
48. Jia, M.; Xu, T.; Li, H. Ecosystem services value of the grain for green program in China—A case study of five representative provinces. *Forests* **2025**, *16*, 1671. [CrossRef]
49. Viña, A.; McConnell, W.J.; Yang, H.; Xu, Z.; Liu, J. Effects of conservation policy on China's forest recovery. *Sci. Adv.* **2016**, *2*, e1500965. [CrossRef]
50. Mao, C.; Tong, X.; Brandt, M.; Yue, Y.; Zhang, W.; Lu, J.; Huang, K.; Wang, K. How three decades of forestation has impacted forest fragmentation in southern China. *Remote Sens.* **2025**, *17*, 1922. [CrossRef]
51. Danylo, O.; Pirker, J.; Lemoine, G.; Ceccherini, G.; See, L.; McCallum, I.; Hadi, H.; Kraxner, F.; Achard, F.; Fritz, S. A map of the extent and year of detection of oil palm plantations in Indonesia, Malaysia and Thailand. *Sci. Data* **2021**, *8*, 96. [CrossRef]
52. Xie, L.; Berck, P.; Xu, J. The effect on forestation of the collective forest tenure reform in China. *China Econ. Rev.* **2016**, *38*, 116–129. [CrossRef]
53. Zhang, H.; Buongiorno, J. Markets, government policy, and China's timber supply. *Silva Fenn.* **2012**, *46*, 595–608. [CrossRef]

Disclaimer/Publisher's Note: The statements, opinions and data contained in all publications are solely those of the individual author(s) and contributor(s) and not of MDPI and/or the editor(s). MDPI and/or the editor(s) disclaim responsibility for any injury to people or property resulting from any ideas, methods, instructions or products referred to in the content.